J. Plasma Phys. (2015), *vol.* 81, 495810511 © Cambridge University Press 2015
doi:10.1017/S0022377815000859

Effect of initial conditions on electron–plasma turbulence: a multiresolution analysis

S. Chen[1,2,†], G. Maero[3,2] and M. Romé[3,2]

[1]Institute of Fluid Physics, China Academy of Engineering Physics, Mianyang, Sichuan 621900, PR China

[2]INFN Sezione di Milano, Via Celoria 16, 20133 Milano, Italy

[3]Dipartimento di Fisica, Università degli Studi di Milano, Via Celoria 16, 20133 Milano, Italy

(Received 31 March 2015; revised 19 June 2015; accepted 19 June 2015)

The transverse dynamics of a pure electron plasma confined in a Penning–Malmberg trap is investigated, taking advantage of two-dimensional particle-in-cell numerical simulations. The evolution of the electron plasma turbulence is studied by means of a wavelet-based multiresolution analysis. In particular, a modified recursive denoising algorithm is developed to separate coherent and incoherent (not necessarily homogeneous) components of the flow. A set of simulations have been carried out changing systematically the radii of an initial annular density distribution of the electrons. The results of the multiresolution analysis indicate that the initial density configuration may have a considerable effect on the evolution of turbulence. Even very small initial density fluctuations can lead to quite different final states, especially in the presence of multiple active diocotron modes characterized by similar growth rates.

1. Introduction

Strongly magnetized pure electron plasmas confined in Penning–Malmberg traps (Malmberg & deGrassie 1975) are excellent systems for quantitative investigations of two-dimensional (2D) fluid dynamic phenomena, such as vortex dynamics and turbulence (Driscoll *et al.* 1999; Durkin & Fajans 2000). With respect to other systems investigated in fluid turbulence studies, such as rotating tanks (Baroud *et al.* 2002), soap films (Rutgers 1998) and electrolyte layers (Rivera, Vorobieff & Ecke 1998), non-ideal effects are significantly reduced for electron plasmas (Romé & Lepreti 2011), allowing for a more direct comparison between experiments and theoretical models.

Namely, under typical experimental conditions, the cold non-relativistic guiding centre approximation holds, and the transverse dynamics of the electron plasma in the trap can be well described by the drift Poisson equations (Driscoll & Fine 1990),

$$\partial n/\partial t + \boldsymbol{v}\cdot\boldsymbol{\nabla} n = 0, \quad \boldsymbol{v} = -\boldsymbol{\nabla}\phi\times\boldsymbol{e}_z/B, \quad \nabla^2\phi = en/\epsilon_0, \tag{1.1a–c}$$

where n is the plasma density, ϕ the electrostatic potential, $\boldsymbol{v}$ the velocity field, B the magnetic field strength, $-e$ the electron charge, ϵ_0 the vacuum permittivity and $\boldsymbol{e}_z$ the

† Email address for correspondence: Chi.Chen@mi.infn.it

https://doi.org/10.1017/S0022377815000859 Published online by Cambridge University Press

unit vector in the axial direction. Equations (1.1) are isomorphic to the Euler equations for an ideal (incompressible, inviscid) fluid (Levy 1965), with vorticity $\zeta = en/\epsilon_0 B$ and stream function $\psi = \phi/B$. Such experimental systems can also be simulated to a high degree of accuracy and with a very efficient computational cost. Several approaches have been used to this aim, such as particle-in-cell (PIC) (Delzanno, Lapenta & Finn 2002; Maero *et al.* 2014), Poisson–Vlasov (Romé *et al.* 2000) and contour dynamics (Coppa, Peano & Peinetti 2002) methods.

One of the most important features of 2D turbulence is the development of coherent vortices from smaller-scale structures: the energy eventually concentrates in large-scale structures by complex vortex interactions, the merger of two like-signed vortices being the fundamental mechanism of vortex growth. Generally, three stages can be observed during the decay of a 2D turbulent flow. The initial stage is characterized by the self-organization of the fluid into a collection of coherent structures containing most of the surviving vorticity. The intermediate stage is governed primarily by two processes: (*a*) mutual advection of the vortices when they are well separated and (*b*) interaction of vortices when they become close. The basis for these processes is the Kelvin–Helmholtz (also called diocotron, in the context of trapped plasmas) fluid instability. As such, these phenomena are relevant to an even wider class of natural contexts, such as astrophysical plasmas (Borgogno *et al.* 2015). Note that in the case of an electron plasma the vorticity has a definite sign. A class of interactions in the evolution of the fluid system is thus excluded.

The free relaxation of 2D turbulence has been described in the literature using, for example, variational principles based on the minimization of enstrophy (Leith 1984; Huang & Driscoll 1994) or the maximization of entropy (Miller 1990; Robert & Sommeria 1991; Miller, Weichman & Cross 1992; Rodgers *et al.* 2009). In the so-called punctuated scaling theory (Carnevale *et al.* 1991; Weiss & McWilliams 1993), the turbulent flow is assumed to be dominated by the presence of strong coherent structures with the occasional mergers of like-signed vortices. In the so-called 'regional' maximum fluid entropy theory (Jin & Dubin 1998, 2000), strong vortices in the flow ergodically mix the background, which in turn cools the chaotic motion of the strong vortices, driving them into an equilibrium pattern. All these statistical theories rely on the presence of global constraints, and usually neglect the details of the early dynamical evolution of the flow. On the other hand, the initial vortex distribution may affect the time evolution of the decaying 2D turbulence, since the vortex interactions strongly depend on vortex size, vorticity amplitude, separation distance of the vortex centres, and background shear induced by the surrounding vortices (Melander, Zabusky & McWilliams 1988; Dritschel & Waugh 1992; Waugh 1992; Amoretti *et al.* 2001; Trieling, Velasco Fuentes & van Heijst 2005). The influence of initial conditions on the evolution of fluid turbulence has been pointed out in several studies (Benzi, Patarnello & Santangelo 1988; Santangelo, Benzi & Legras 1989; Driscoll *et al.* 2000; Yin, Montgomery & Clerckx 2003; Kalelkar 2005; van Bokhoven *et al.* 2007).

In a previous work, the statistical and scaling properties of the 2D turbulence in pure electron plasmas were investigated (Lepreti *et al.* 2013) by analysing the results of experiments carried out in the Penning–Malmberg device ELTRAP (Amoretti *et al.* 2003). It was observed that the intermittency properties of the turbulence strongly depend on the initial conditions. In particular, two types of initial conditions for the electron density, namely annular and spiral configurations, were considered.

In the present paper, we investigate the 2D turbulence in a pure electron plasma by analysing the results of a series of 2D PIC numerical simulations of the plasma

https://doi.org/10.1017/S0022377815000859 Published online by Cambridge University Press

transverse dynamics. A 2D orthogonal wavelet-based multiresolution analysis (MRA) is adopted. In contrast to Fourier transformation, wavelets have well-localized basis functions in both physical and wavenumber space (Farge 1992; Mallat 1999). They therefore allow for a better discrimination of local and non-stationary features of the flow. This property is of relevance, for example, for a correct description of the evolution of a 2D turbulent fluid at very high Reynolds numbers, where long-lived coherent structures with different spatial scales develop, breaking the homogeneity hypothesis (Frisch 1995).

In the following, a systematic investigation of the initial density conditions is performed in order to characterize the parameters playing a major role in the early dynamics of the flow and leading to an evolution dominated either by the presence of coherent structures (persistent vortices) and possibly the formation of vortex crystal-like states, or by a higher turbulence level. An initial annular flat electron density has been assumed in order to have a quantitative comparison with well-known analytical results of the linear evolution stage of azimuthal low-frequency instabilities of the system (Davidson 1990).

The paper is organized as follows. The general case study, the 2D PIC simulations and the wavelet-based MRA method are described in § 2. The main results about the plasma evolution, its turbulent features and the sensitivity on initial conditions are presented in § 3, while § 4 is devoted to conclusions.

2. PIC code and multiresolution analysis

2.1. *PIC simulations*

The transverse dynamics of the electron plasma is simulated using a recently developed 2D PIC code (Maero *et al.* 2014). The code simulates in general the 2D dynamics of a multispecies plasma in the plane orthogonal to a homogeneous magnetic field, implementing a massless fluid approximation for electrons and a kinetic description for the massive components. For the simulations presented here, however, only the electron population is considered.

It is worth noting that, in the case of a pure electron plasma, an Eulerian fluid numerical code could also be used to describe the dynamics of the system (Romé *et al.* 2000), and the Eulerian fluid description would be cleaner from noise than the PIC one. However, the PIC code used here provides us with great flexibility, namely we can (*a*) easily adapt the boundary geometry and initial conditions and (*b*) use both fluid and kinetic trajectory integration routines for different particle populations. The latter feature can be particularly important, e.g. in order to compare the turbulence properties of a pure electron plasma with those of a dust-contaminated electron plasma, where dust grains require a kinetic treatment (Maero *et al.* 2014). Moreover, the PIC noise is useful in the present context to simulate the non-uniformities of the initial electron distribution that are unavoidably present in the experiments, and their influence on the late evolution of the system (see § 3.3).

The plasma domain is supposed to be bounded by a (perfectly) conducting wall of radius R_w. The electrostatic potential ϕ is therefore set to zero on the circular boundary. This corresponds to free-slip boundary conditions in the fluid description. In the PIC code, a Cartesian $N_{grid} \times N_{grid}$ grid, with $N_{grid} = 256$, is used, and the circular boundary is approximated by a piecewise linear function following the sides of the mesh cells. The number of macro-particles, N_{macro}, is 10^6. Using a standard bilinear interpolation for the charge density, the Poisson equation for ϕ is solved by means of a 2D fast Fourier transform (FFT) combined with a capacity matrix method

https://doi.org/10.1017/S0022377815000859 Published online by Cambridge University Press

(Hockney & Eastwood 1981). For the time advancement of the electrons, a fourth-order Runge–Kutta algorithm is adopted.

Equations (1.1) can be written in non-dimensional form as

$$\partial n/\partial t + \boldsymbol{e}_z \times \boldsymbol{\nabla}\phi \cdot \boldsymbol{\nabla} n = 0, \quad \nabla^2\phi = n, \tag{2.1a,b}$$

where the density n is normalized over a reference value n_0, the lengths over the trap radius R_w, the electrostatic potential ϕ over $en_0R_w^2/\epsilon_0$ and the time over $\omega_c/\omega_p^2 = \epsilon_0 B/en_0$, where $\omega_c = eB/m$ is the (non-relativistic) electron cyclotron frequency and $\omega_p = (e^2n_0/\epsilon_0 m)^{1/2}$ is the plasma frequency computed using the density n_0. Simulations performed for the same final time therefore correspond to a given ratio between the density and the magnetic field strength. In the following, only non-dimensional quantities are used. The parameters of the simulations presented here are analogous to those used (in dimensional form) in (Maero *et al.* 2014), and correspond to experimental conditions actually encountered in existing or planned Penning–Malmberg traps (Maggiore *et al.* 2014; Romé *et al.* 2015).

The drift Poisson system (2.1) is Hamiltonian and expresses the fact that the electron density (fluid vorticity) is a Lagrangian invariant, i.e. it is constant along the characteristics given by the $E \times B$ drift. The evolution of the electron density is constrained by an infinite number of constants of motion, known as Casimirs (Morrison 1984), corresponding to integrals over the spatial domain of an arbitrary function of the Lagrangian invariant density. In particular, the enstrophy (Leith 1968) corresponds to the quadratic invariant

$$Z = \frac{1}{2}\int r\,\mathrm{d}r\,\mathrm{d}\theta\, n^2, \tag{2.2}$$

where (r, θ) are polar coordinates defined in the circular domain. These Casimirs are conserved in addition to the total number of particles N_{tot}, the energy H and the angular momentum P_θ (all these quantities are defined per unit axial length). In non-dimensional form these are given by

$$N_{tot} = \int r\,\mathrm{d}r\,\mathrm{d}\theta\, n(r, \theta, t), \tag{2.3}$$

$$H = -\frac{1}{2}\int r\,\mathrm{d}r\,\mathrm{d}\theta\, n(r, \theta, t)\phi(r, \theta, t) = \int r\,\mathrm{d}r\,\mathrm{d}\theta\, |\boldsymbol{\nabla}\phi(r, \theta, t)|^2, \tag{2.4}$$

$$P_\theta = -\frac{1}{2}\int r\,\mathrm{d}r\,\mathrm{d}\theta\, r^2 n(r, \theta, t). \tag{2.5}$$

In the fluid analogy, the corresponding quantities are the total circulation, the excess kinetic energy and the total angular impulse, respectively (Melander *et al.* 1988). In the simulations presented here, H and P_θ are typically conserved with a relative accuracy of the order of 10^{-5} and 10^{-6}, respectively, for a time equivalent to more than a hundred plasma rotation periods. On the contrary, the total enstrophy Z and in general all other higher moments of the vorticity tend to decrease with time. This effect is due to 'coarse-graining', as observed both in experiments and in numerical simulations (Schecter *et al.* 1999): the density (vorticity) filaments become longer and longer so that their thickness becomes smaller than the experimental resolution (e.g. the pixel size of the optical diagnostics of the density) or smaller than the cell size of the numerical mesh used for the discretization of the 2D Euler equations,

https://doi.org/10.1017/S0022377815000859 Published online by Cambridge University Press

respectively. This effect of coarse-graining on the invariants of the 2D Euler equations has been pointed out also in statistical treatments of the 2D turbulence (Miller 1990).

The initial electron density distribution is assumed to be uniform over an annular region. This kind of density distribution can be easily produced in the experiments (Peurrung & Fajans 1993) and it also allows for a quantitative comparison with analytical results of the linear evolution stage of azimuthal low-frequency instabilities of the system (Davidson 1990). In order to investigate the influence of the initial distribution on the evolution of the plasma turbulence, the same uniform density and the same total number of particles N_{tot} are considered in all simulations. This is accomplished by keeping the total initial area A covered by the plasmas constant, and varying the outer radius r^+ of the annulus (and correspondingly its inner radius r^-) in a given range. As a reference value, $A = 0.0729\pi$ has been chosen, i.e. a fraction of slightly more than 7 % of the total cross-section of the trap is supposed to be initially filled by the plasma. The various cases therefore differ for the profile of the shear of the rotation angular frequency, $r\,\mathrm{d}\omega_r/\mathrm{d}r = (r^-/r)^2$, inside the plasma (the rotation frequency ω_r being normalized over ω_p^2/ω_c), and for the value of the canonical angular momentum P_θ and of the energy H. With $N_{macro} = 10^6$, the number of simulation particles per occupied cell for the initial condition is typically greater than 250, which guarantees a good level of density uniformity over the area initially covered by the plasma (see discussion on this point in § 3.3).

2.2. *Wavelet multiresolution analysis*

A wavelet-based MRA method is applied in order to separate the coherent structures (persistent vortices) from the incoherent vorticity distribution and to perform a spectral analysis on the coherent and incoherent parts of the flow. The 'signal', i.e. the 2D vorticity (density) distribution at a given time of the evolution, is successively decomposed into coefficients that contain coarse and fine details at increasingly finer resolution. The 2D vorticity field is expanded as

$$\zeta(x, y) = \overline{\zeta}_{0,0,0}\phi_{0,0,0}(x, y) + \sum_{j=0}^{J-1}\sum_{i_x=0}^{2^j-1}\sum_{i_y=0}^{2^j-1}\sum_{\sigma=1}^{3}\tilde{\zeta}^{\sigma}_{j,i_x,i_y}\psi^{\sigma}_{j,i_x,i_y}(x, y), \tag{2.6}$$

i.e. as a linear combination of elementary well-localized functions $\psi^{\sigma}_{j,i_x,i_y}(x, y)$ (here a Symlet8 wavelet has been chosen), with coefficients $\tilde{\zeta}^{\sigma}_{j,i_x,i_y}$. These wavelet coefficients are then separated into coherent and incoherent parts, using an adaptive, self-consistent universal Donoho's threshold within an iterative method (Farge, Schneider & Kevlahan 1999; Ruppert-Felsot, Farge & Petitjeans 2009). The method is similar to the one applied in a previous work (Bettega, Pozzoli & Romé 2009) for the analysis of experimental time sequences of the electron density distribution, where it was shown that most of the information about the 2D flow is retained in a small fraction of the coefficients describing the coherent part.

In the present work, the method has been modified in order to take into account a possible inhomogeneity of the incoherent part. In the usually adopted method (Ruppert-Felsot *et al.* 2009), the incoherent part $\zeta_<$ at the ith iteration step is reconstructed using wavelet coefficients smaller (in absolute value) than a threshold $\epsilon_T^{(i)}$ (which is computed at the previous step). Its variance $\langle\zeta_<^2\rangle = (1/N_{grid}^2)\sum\zeta_<^2(x, y)$ is then used to compute the new threshold $\epsilon_T^{(i+1)} = (2\langle\zeta_<^2\rangle \log N_{grid}^2)^{1/2}$ at the next step. At the first iteration, $\epsilon_T^{(1)} = (2\langle\zeta^2\rangle \log N_{grid}^2)^{1/2}$, where $\langle\zeta^2\rangle$ is the variance of the total signal. The method works well, i.e. the threshold stabilizes (indicating convergence)

https://doi.org/10.1017/S0022377815000859 Published online by Cambridge University Press

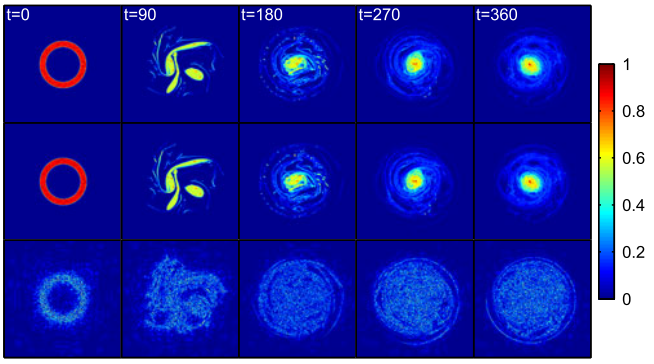


FIGURE 1. Results of the modified wavelet MRA for $r^+ = 0.40$. The top, middle and bottom rows show the absolute values of the total, coherent and incoherent parts, respectively. In each plot the data are normalized to their respective maximum values. Each column corresponds to a different time, namely $t = 0$, 90, 180, 270 and 360, as indicated at the upper-left corner of each plot in the top row.

after a few iterations, $|\epsilon_T^{(i+1)} - \epsilon_T^{(i)}| \approx 0$, and the coherent and incoherent parts are then separated, for the cases where the incoherent part can be regarded as an additive Gaussian noise homogeneously distributed over all grid points. However, if the incoherent part is highly inhomogeneous and actually covers only a small fraction of the grid points, the threshold fails to converge. The reason for this failure is as follows. On the one hand, convergence of the threshold requires the variance of the incoherent part $\langle \zeta_<^2 \rangle$ to be similar to the intrinsic variance σ_G^2 of a Gaussian noise. On the other hand, $\langle \zeta_<^2 \rangle$ (and thus ϵ_T) depends not only on its intrinsic statistical properties, but also on a geometric factor: the ratio of the area covered by the incoherent part to the total signal domain. When the incoherent part is distributed over all (or most of) the grid points, this ratio is approximately equal to 1, and $\langle \zeta_<^2 \rangle \approx \sigma_G^2$. If, however, the incoherent part is inhomogeneously distributed, the geometric factor can be much smaller than 1 (e.g. at the initial time it is approximately 7 %, as mentioned above, since it corresponds to the percentage of the domain where the signal is effectively non-zero), resulting in $\langle \zeta_<^2 \rangle \ll \sigma_G^2$. In the latter case, the requirement for the threshold convergence is violated and the algorithm fails. In order to relax this restriction, we considered at each step the relative change of the threshold, $\Delta\hat{\epsilon}_T^{(i)} = [\epsilon_T^{(i+1)} - \epsilon_T^{(i)}]/\epsilon_T^{(i)}$. Unlike ϵ_T, $\Delta\hat{\epsilon}_T$ does not depend on the geometric factor, and ensures that at a certain step $|\Delta\hat{\epsilon}_T^{(i_0+1)} - \Delta\hat{\epsilon}_T^{(i_0)}| \approx 0$. Then we can use the corresponding threshold $\epsilon_T^{(i_0)}$ to separate the coherent and incoherent parts. Using this modified algorithm, we can retain the hypothesis of Gaussianity of the incoherent part, while relaxing the requirement that it covers the entire signal domain.

To demonstrate its performance, we present in figure 1 the results of this modified algorithm applied to the case of $r^+ = 0.40$. The top, middle and bottom rows show the absolute values of the total, coherent and incoherent parts of the density distribution, respectively, while each column corresponds to a different time. For the sake of clarity, all distributions are normalized to their respective maximum values. The evolution of the total and/or the coherent vorticity field will be discussed in detail in the following sections. The incoherent part is inhomogeneous at early times (e.g. $t = 0$ and 90), but acquires a higher degree of homogeneity at later times (from $t = 180$ to 360). On the other hand, the values of the incoherent part turn out to be randomly distributed

https://doi.org/10.1017/S0022377815000859 Published online by Cambridge University Press

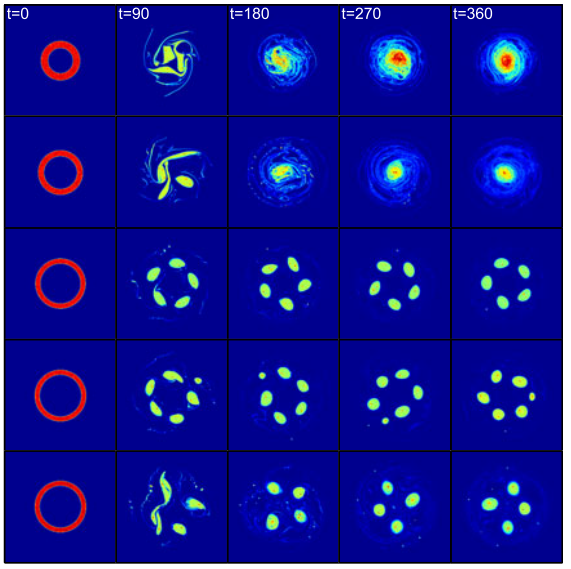


FIGURE 2. Time evolutions of the electron density (vorticity). Each row corresponds to a given value of the outer radius of the initial annulus: $r^+ = 0.35$, 0.40, 0.45 and 0.46 (last two rows). Each column corresponds to a different (normalized) time, as indicated at the upper left corner of each plot in the first row.

throughout all the time evolution. These features confirm that the modified algorithm described above is able to separate the inhomogeneous incoherent part. It is also worth noting that, as the system evolves towards its final state, a nearly uniform turbulent background is formed, even in the presence of a central vortex patch. This result will be discussed further in § 3.2. Further technical details about the modified method of separation of the coherent and incoherent parts of the flow will be reported in a future paper. Despite its possible inhomogeneity, the incoherent part can still be considered as a Gaussian noise, and the main interest of the present work remains in the coherent part.

3. Effect of initial conditions

3.1. *Emergence of different final states*

As mentioned in the previous section, we choose the outer radius r^+ of the annulus as the freely varying parameter. A series of simulations are performed in which r^+ is systematically changed from 0.35 to 0.46 with an increment of 0.01. The evolutions of the vorticity for different values of r^+ are shown in figure 2. Each row corresponds to a given value of r^+, while each column corresponds to a different time.

The numerical results show in general typical fluid phenomena like the development of the diocotron instability (Kelvin–Helmholtz instability in the fluid language), vortex merging events, the emission of vorticity filaments and the development of a turbulent background. In all cases there is a first stage characterized by the development of the diocotron instability, which leads to the breakup of the annulus into several vortices. After this stage, however, the evolution of plasma changes drastically as r^+ increases, leading to quite different final states. For smaller r^+, the final state consists of a single

https://doi.org/10.1017/S0022377815000859 Published online by Cambridge University Press

central patch and a turbulent background, while for larger r^+ final states with multiple vortices can emerge.

We have performed an analysis of the early evolution of the diocotron instability to extract the growth rate γ_l of the lth mode from the simulation data and to compare the results with the theoretical predictions based on a linear perturbation analysis (Davidson 1990). The electron density and the electrostatic potential at any time t can be Fourier-analysed as

$$n(r, \theta, t) = \sum_{l=-\infty}^{+\infty} n_l(r) \mathrm{e}^{\mathrm{i}(l\theta - \omega_l t)}, \tag{3.1}$$

$$\phi(r, \theta, t) = \sum_{l=-\infty}^{+\infty} \phi_l(r) \mathrm{e}^{\mathrm{i}(l\theta - \omega_l t)}, \tag{3.2}$$

where ω_l is a complex frequency. The diocotron mode of order l is unstable if $\gamma_l = \mathrm{Im}(\omega_l) > 0$: this also defines the growth rate of the mode. Accordingly, the electrostatic energy contained in the lth mode is

$$E_l(t) = -2\pi \int_0^1 \mathrm{Re}[n^l(r)\phi_l^*(r)]\mathrm{e}^{2\gamma_l t} r \, \mathrm{d}r, \tag{3.3}$$

where the asterisk denotes the complex conjugate. In practice, the density and potential at time t are calculated on a polar grid starting from the instantaneous particle distributions, and their Fourier components are used to evaluate the electrostatic energy $E_l(t)$. Fitting $E_l(t)$ to an exponential function yields the growth rate $2\gamma_l$. Alternatively, one can calculate the power $A_l(t)$ of the lth mode,

$$A_l(t) = 2\pi \int_0^1 |\delta\phi_l(r, t)|^2 r \, \mathrm{d}r, \tag{3.4}$$

where $\delta\phi_l(r, t)$ denotes the lth Fourier component of the potential perturbation, and carry out a similar exponential fitting of $A_l(t)$ (Maero *et al.* 2014). The numerical growth rates obtained by these two methods agree well with each other, and hereafter we report the results obtained using the former one.

In table 1 we list the exponential growth rates γ_l for $l = 1$–10 for a few values of r^+. The growth rates are normalized by the diocotron frequency $\omega_D = \omega_p^2/2\omega_c$. The dominant mode (indicated in bold) progressively changes from $l = 3$ to $l = 4$ and finally to $l = 5$. In figure 3 we plot the dominant diocotron mode number in the final state versus the outer radius r^+. The solid circles represent final states with a single central vortex. Since these states are approximately axisymmetric, they are characterized by $l = 0$. The solid squares, on the contrary, represent multiple-vortex final states with non-zero mode numbers. Representative vorticity distributions during the diocotron instability stage are also shown (see insets). It is well known that the instability occurs at higher azimuthal mode numbers when the plasma annulus becomes thinner (Davidson 1990). In the present study, as r^+ increases, the width of the annulus decreases, and the mode with the largest growth rate therefore shifts to a higher l. It turns out that, for cases with low-order dominant diocotron modes, vortex merging processes dominate the plasma evolution up to the formation of a single central vortex. In the opposite case, i.e. for higher-order dominant diocotron modes, vortex merging processes can be largely suppressed, and the initially dominant

https://doi.org/10.1017/S0022377815000859 Published online by Cambridge University Press

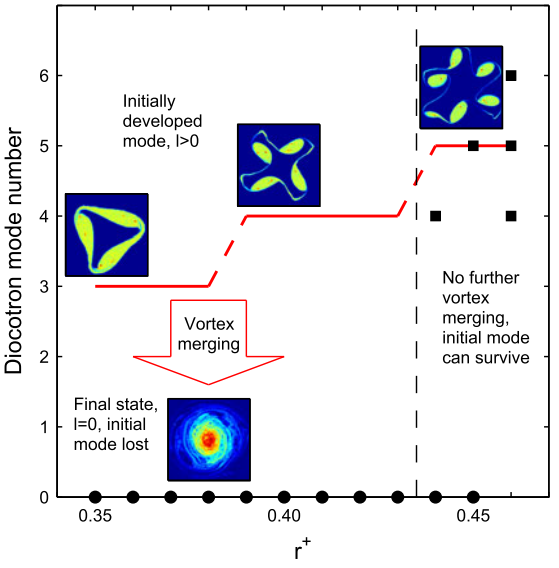


FIGURE 3. Azimuthal mode number of the dominant diocotron mode in the final state versus the normalized outer radius r^+. The solid circles and squares represent final states with a single central vortex and with multiple vortices, respectively. The red lines indicate the dominant modes for different r^+ as predicted from the linear theory (Davidson 1990). Insets show examples of vorticity distributions during the diocotron instability stage.

r^+	γ_l/ω_D									
	$l=1$	$l=2$	$l=3$	$l=4$	$l=5$	$l=6$	$l=7$	$l=8$	$l=9$	$l=10$
0.35	—	0.0460	**0.2341**	—	—	—	—	—	—	—
	0.1030	0.0913	**0.2258**	—	—	—	—	—	—	—
0.40	—	0.0530	0.2476	**0.2827**	0.1687	—	—	—	—	—
	0.1090	0.1024	0.2328	**0.2583**	0.1860	—	—	—	—	—
0.45	—	0.0570	0.2258	*0.2989*	**0.3120**	0.2496	—	—	—	—
	0.1355	0.1778	0.2021	*0.2437*	**0.2905**	0.2431	—	—	—	—
0.46	—	0.0576	0.2206	*0.2965*	**0.3190**	*0.2796*	0.0981	—	—	—
	0.1290	0.1995	0.2204	*0.2621*	**0.2912**	*0.2674*	0.1909	—	—	—

TABLE 1. Growth rate γ_l (normalized to ω_D) of the diocotron modes for different values of r^+. For each radius, the values in the first row are the analytical predictions of the linear perturbation theory (Davidson 1990), while the values in the second row are obtained by the Fourier analysis of the results of the numerical simulations. The growth rate of the dominant mode is indicated in **bold**. The growth rates of other modes that are only slightly smaller than that of the dominant one are indicated in *italic*. Stable modes are represented by dashes.

mode leads to the formation of a chain of vortices (vortex crystal), characterized by a number of vortices equal to the order of the same dominant mode.

In order to investigate in more detail the time evolution of the plasma turbulence, we compare the vorticity distribution as well as the enstrophy spectrum of the coherent part for two qualitatively different cases, namely $r^+ = 0.40$ and $r^+ = 0.46$.

https://doi.org/10.1017/S0022377815000859 Published online by Cambridge University Press

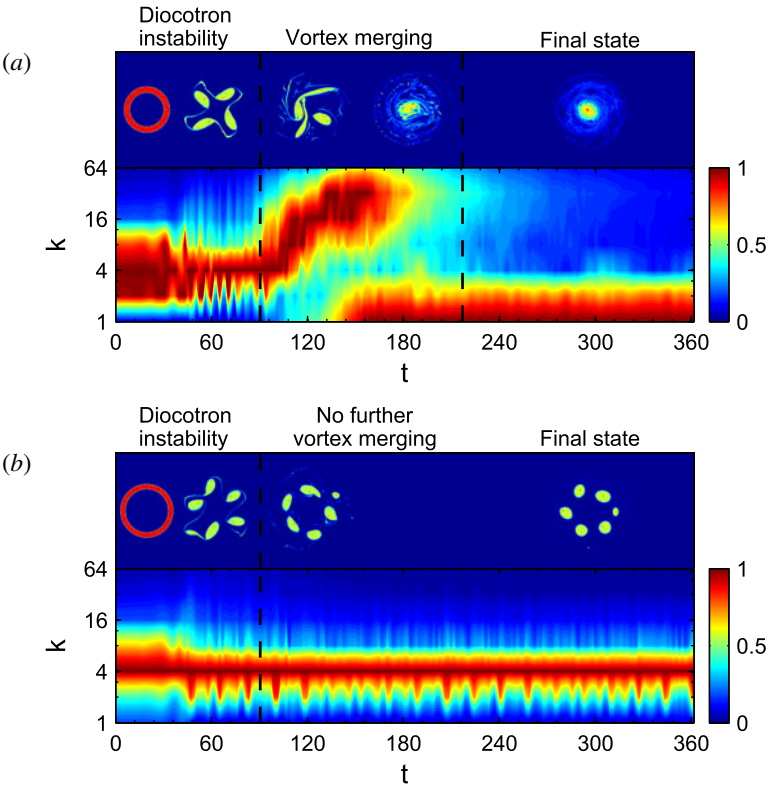


FIGURE 4. Comparison of vorticity distribution and enstrophy spectrum of the coherent part between (*a*) $r^+ = 0.40$ and (*b*) $r^+ = 0.46$. The enstrophy spectrum is normalized by its maximum value at each time. In (*a*), the three main stages (i.e. development of diocotron instability, vortex merging and final state) are separated by two vertical dashed lines, while in (*b*) the vortex merging stage is absent.

The maximum wavenumber k_{max} of the spectrum is the inverse of the minimum spatial scale of the wavelet functions (which is twice the length of a grid cell), i.e. $k_{max} = 1/[2 \times (2/N_{grid})] = 64$ (the wavenumber is normalized over the inverse of the trap wall radius, $1/R_w$). In each successive decomposition level the spatial scale of the wavelet functions is increased by a factor of 2 and k is accordingly divided by 2, up to a maximum level of $(\log_2 N_{grid} - 1) = 7$, i.e. up to a minimum wavenumber $k_{min} = 1$.

For $r^+ = 0.40$ (see figure 4*a*), we can distinguish three main stages. The first stage corresponds to the above-mentioned evolution of the diocotron instability, during which the annulus breaks into multiple (e.g. four in this case) vortices. The second stage lasts until the formation of a single vortex state. During this stage the vortices interact strongly with each other, undergoing vortex merging and emission of vorticity filaments. As a consequence of these processes, the vortices collapse into a single central patch, and a significant turbulent background is formed. It is worth noting that this stage can be distinguished not only from the visible evolution of the vorticity distribution, but also from a 'bifurcation' structure in the coherent enstrophy spectrum (as discussed in detail in § 3.2). After this stage both the vorticity distribution and the coherent enstrophy spectrum remain relatively stable, without further evolution.

https://doi.org/10.1017/S0022377815000859 Published online by Cambridge University Press

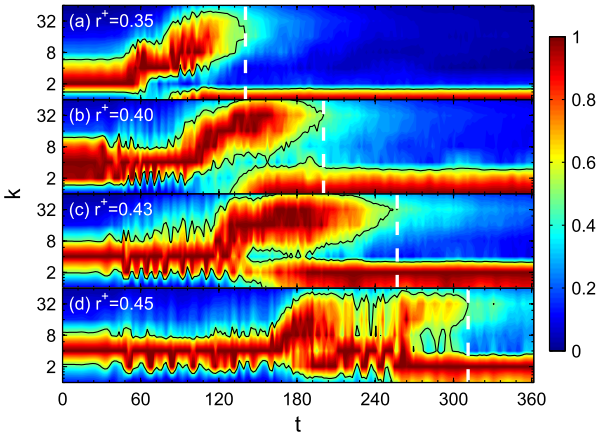


FIGURE 5. Coherent enstrophy spectrum for different initial outer radii of the plasma annulus, as indicated at the upper left corner of each plot. The spectrum is normalized by its maximum value at each time. The vortex merging stage corresponds to the period in which the spectrum shows a bifurcating structure. When the vortex filaments lose their identity into a turbulent background, the upper branch at larger wavenumbers disappears. The instant at which the upper branch falls completely below the value 0.5 (indicated by the black contour lines) is regarded as the typical time of turbulence development, T_{turb} (indicated by the white dashed lines).

On the other hand, it is clear from figure 4(*b*) that for $r^+ = 0.46$ the second stage is absent. The multiple vortices formed after the diocotron instability evolution do not merge with each other and the emission of the vorticity filaments is greatly reduced.

3.2. *Development of turbulence*

As mentioned before, during the vortex merging stage the vortices generated from the diocotron instability interact with each other, collapse into a central vortex, and generate a strong turbulent background. This implies that the vortex merging process is closely related to the development of turbulence, as discussed in the following.

In figure 5 we compare the evolution of the enstrophy spectrum of the coherent component for different r^+. A common feature is that the vortex merging stage corresponds to the period in which the spectrum shows a 'bifurcation' structure. During the diocotron instability stage, the annulus breaks into several vortices, but the spatial scale of these vortices remains roughly the same as that of the annulus. Therefore, the peak of the enstrophy spectrum (indicated by the red region) remains close to its initial position during this period. However, during the merging process the vortices become highly deformed, and emit vortex filaments. In the meantime the enstrophy is transferred into components of both larger (central vortex) and smaller (vortex filaments) spatial scales. This corresponds to the bifurcation of the spectrum. At the end of the merging stage, vortex filaments evolve into a turbulent background, losing their identity. Thus, the upper branch at larger wavenumbers (i.e. smaller spatial scales) disappears in the spectrum of the coherent part of the flow and only the lower branch at smaller wavenumbers (i.e. larger spatial scales) remains. The time T_{turb} at which the upper branch vanishes can be regarded as the typical time of turbulence development. This time is estimated from the coherent enstrophy spectrum

https://doi.org/10.1017/S0022377815000859 Published online by Cambridge University Press

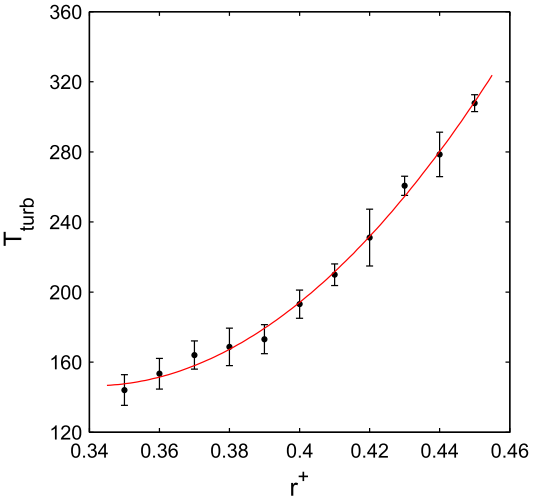


FIGURE 6. Relation between the typical time of turbulence development T_{turb} and the outer radius r^+. The solid line is a quadratic fit.

as the instant at which the upper branch falls completely below a given value, which we set here to 0.5. Notice the black contour lines for the level 0.5 and the white dashed lines indicating T_{turb} in figure 5.

The comparison between the spectrum evolution for different initial outer radii in figure 5 implies that T_{turb} increases with r^+. In figure 6 we show the relation between T_{turb} and r^+. Several (at least four) simulations are actually carried out for a given r^+, so that the average of the values of T_{turb} obtained in all these simulations is shown in the plot, together with an error bar corresponding to one standard deviation. It is confirmed that, as r^+ increases, it takes more time for turbulence to fully develop. Several considerations qualitatively support and clarify this evidence. First, as the outer radius increases, the effective area that can be covered by the turbulent background also increases. Namely, the vortex filaments become thinner and thinner with time and the strong vortices tend to move towards the centre, while the canonical angular momentum of the system is kept constant during the evolution. This effect explains the growth of T_{turb} since the time needed to obtain an almost uniform background increases, as already shown in figure 1. Second, as the dominant mode shifts to higher mode numbers, more vortices are generated before the vortex merging stage actually begins. The typical size of these vortices becomes smaller, while the average distance between the vortices gets larger, so that it takes more time for vortex merging to complete, and the evolution of turbulence is slowed down. This effect contributes to the increase of the slope of T_{turb} with r^+. One can also consider that the area to be covered by the turbulent background increases with the square of r^+ and it is therefore reasonable to expect a quadratic trend for T_{turb}. Indeed, the solid fitted line in figure 6 shows that the data are compatible with a quadratic dependence with the outer ring radius.

3.3. *Effect of initial fluctuations*

In the PIC simulations the initial particle positions are given using a Mersenne Twister (Matsumoto & Nishimura 1998) random number generator (RNG). As with any RNG,

https://doi.org/10.1017/S0022377815000859 Published online by Cambridge University Press

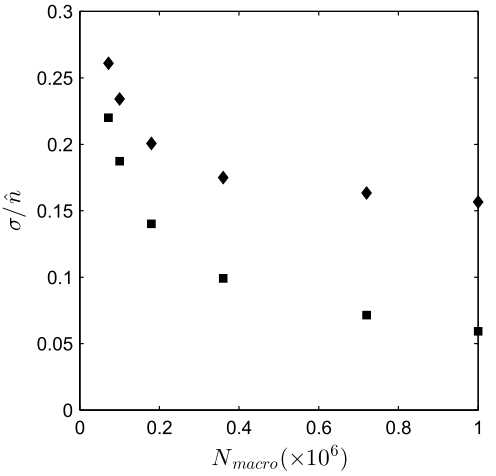


FIGURE 7. Standard deviation σ of the macro-particle distribution normalized over the average number of macro-particles per cell $\hat{n}$ versus the total number of macro-particles N_{macro} for a square (square markers) and a circular (diamond markers) distribution.

fluctuations are introduced into the initial density distribution. To estimate the degree of non-uniformity of the initial particle distribution, we computed for different geometries and different N_{macro} the distributions of the number of macro-particles per cell. Indicating with n_i the number of macro-particles in the ith cell and with $\hat{n}$ its average value, the standard deviation σ of the macro-particle distribution is computed as

$$\sigma^2 = \frac{1}{N_{cell}} \sum_{i=1}^{N_{cell}} (n_i - \hat{n})^2, \tag{3.5}$$

where N_{cell} is the number of grid cells over which the distribution of macro-particles is defined. As an example, in figure 7 the normalized standard deviation $\sigma/\hat{n}$ is shown for different values of N_{macro} for a distribution in a square (square markers) and in a circular region (diamond markers), respectively. In both cases, $N_{grid} = 256$ has been used and the particles have been generated in a test region located at the centre of the domain, covering about the same fraction of the total computational area as that initially covered by the plasma in the previously reported simulations. For the square distribution the boundary of the test region is assumed to coincide with the sides of the mesh cells.

In the case of the square distribution, the relative standard deviation decreases as $1/\sqrt{N_{macro}}$ and is approximately 5 % for $N_{macro} = 10^6$, which is the number of macro-particles used in the simulations reported in the paper. In this case the fluctuations of the particle distribution are due simply to the intrinsic non-uniformity of the RNG. On the contrary, the decrease of $\sigma/\hat{n}$ with N_{macro} turns out to be much slower in the case of the circular distribution. Here, the particles are covering a region whose boundary does not coincide with the sides of the mesh cells. In other words, the mesh cells located at the boundaries of the region occupied by the initial distribution have a smaller n_i with respect to the cells in the interior. For a given N_{macro} the average number of macro-particles per cell $\hat{n}$ is therefore reduced with respect to the square distribution and σ increases. In this case the fluctuations of the particle distribution are mainly due to the discretization of the system.

https://doi.org/10.1017/S0022377815000859 Published online by Cambridge University Press

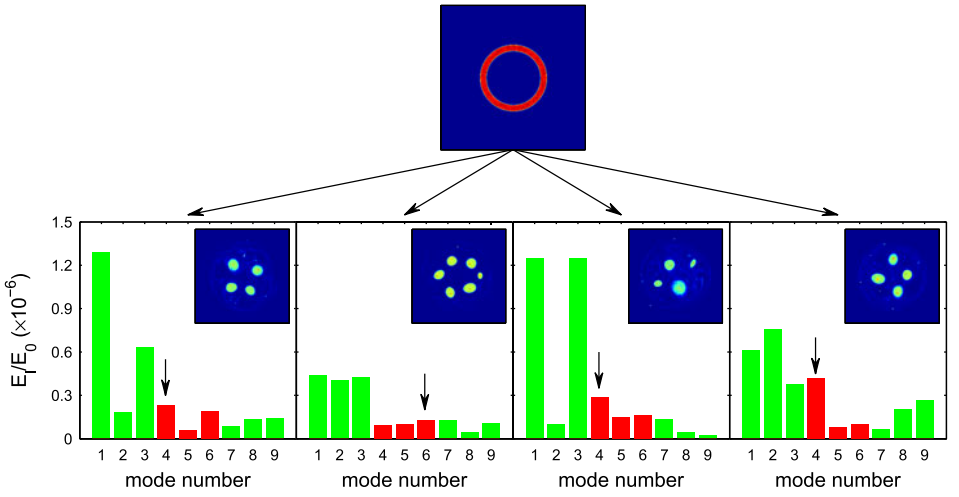


FIGURE 8. Effect of initial fluctuations for 'sensitive' cases where multiple competing diocotron modes exist. The red bars indicate the competing modes and the green ones the other modes. The competing mode with the largest initial energy (indicated by the arrow) survives in the final state (see insets).

Albeit almost unavoidable, these fluctuations have often been neglected or scarcely considered. The effect of fluctuations at lower macro-particle density can sometimes be masked by intentional spatial or density perturbations superimposed on the initial distributions, as customary in some studies of the diocotron instability (see for instance Delzanno *et al.* 2002). Nevertheless, such imperfections may have a significant effect on the fluid dynamics, as we show in the following. Furthermore, although different in nature, they have an equivalent counterpart in real experiments, where particle sources have an intrinsically limited degree of uniformity and reproducibility. Hence the effect of initial fluctuation is not only of numerical interest, but also of practical significance (Yatsuyanagi *et al.* 2003). It is found that for cases with small r^+ initial fluctuations have a negligible effect on the plasma evolution. The analysis of vorticity distribution, enstrophy spectrum, probability distribution function and other quantities shows only minor differences between different runs performed with the same macroscopic parameters. On the other hand, for cases with large r^+, even very small initial fluctuations can lead to quite different plasma evolutions. For example, the results of four runs with $r^+ = 0.46$ are shown in figure 8: three runs end up with four vortices and one run with six vortices. A similar situation is observed for $r^+ = 0.45$ (not shown here), where the system evolves to a single central vortex in two runs, and to a final state with four vortices in two other runs.

Such an effect of initial fluctuations can be explained according to the diocotron instability theory. As shown in table 1, for small r^+ fewer modes are unstable and the growth rate of the dominant mode is much larger than that of all other modes. Thus it will always survive the diocotron instability stage, regardless of the presence of fluctuations. In these cases (which we call 'insensitive'), the effect of initial fluctuations is negligible. For large r^+, on the other hand, the growth rate of the dominant mode is only slightly greater than that of the second and/or third fastest ones. Since these modes are competing, each of them has the possibility to survive the diocotron instability stage. In these cases (which we call 'sensitive'), the

https://doi.org/10.1017/S0022377815000859 Published online by Cambridge University Press

development of the diocotron instability depends not only on the growth rate but also on the initial energy of these competing modes. In order to clarify this point, we take $r^+ = 0.46$ as an example, and use (3.3) to calculate the initial energies E_l of the lth mode for all four runs. As fluctuations eventually contribute to $l > 0$ modes, E_l with $l = 1$–9 (normalized by the initial energy E_0 of the $l = 0$ mode) are shown in figure 8. The competing modes are indicated by red bars. It is clear that the competing mode with the largest initial energy survives up to the final state, which confirms the effect of the initial fluctuations mentioned above.

4. Conclusions

The 2D electron plasma turbulence has been investigated by means of 2D PIC simulation and a wavelet-based multiresolution analysis. The results indicate that the initial conditions indeed have a considerable effect on the evolution of the 2D turbulence with large deviations with respect to the predictions made on the basis of the linear stage mode growth rates. Specifically, the fully nonlinear dynamics (e.g. the typical time of turbulence development) and the final equilibrium states are heavily affected.

Increasing the outer radius of the initial annular density (vorticity) distribution shifts the active diocotron modes towards higher mode numbers, creating more vortices of smaller spatial sizes at the end of diocotron instability stage, and suppressing vortex merger processes. As a result, the final state changes from a single central patch to a multiple-vortex pattern. Even for the cases where the final state remains as a single central patch together with a turbulent background, the typical time to reach equilibrium (or equivalently, the time required to achieve a state of fully developed turbulence) increases with the initial outer radius. It was shown that for cases where multiple diocotron modes with similar growth rates are competing, the survival of a given mode up to the final state depends not only on its growth rate, but also on its initial energy which is introduced by fluctuations.

In such cases, the turbulence evolution is ‘sensitive’ to these initial fluctuations: the same initial macroscopic density (vorticity) distribution could lead to different final states (usually consisting of different number of persistent vortices). Since fluctuations are almost unavoidable in both numerical simulations (due to the intrinsic non-uniformity of RNGs and the discretization of the system) and experiments (e.g. due to small difference of temperature, density, thickness or impurity level of thermionic electron sources), studies on their effects are of both numerical and practical significance.

The complete understanding of some features described here requires further investigations, in terms of both simulation and modelling. An example is the correlation between the turbulence development time and the initial spatial configuration of the plasma distribution, where it is evident that vortex merger process plays an essential role. Another test of these observations may come from the study of different initial conditions (multiple annuli or spirals) where a larger number of vortices is formed and intermittency phenomena were evidenced by MRA and statistical analysis techniques (Romé & Lepreti 2011; Lepreti *et al.* 2013).

Acknowledgements

This work is partially supported by NSFC (nos 11204281 and 11302202) and by the INFN Group V within the ‘COOLBEAM’ project.

https://doi.org/10.1017/S0022377815000859 Published online by Cambridge University Press

REFERENCES

AMORETTI, M., BETTEGA, G., CAVALIERE, F., CAVENAGO, M., DE LUCA, F., POZZOLI, R. & ROMÉ, M. 2003 Cylindrical Penning trap for the study of electron plasmas. *Rev. Sci. Instrum.* **74** (9), 3991–3997.

AMORETTI, M., DURKIN, D., FAJANS, J., POZZOLI, R. & ROMÉ, M. 2001 Asymmetric vortex merger: experiments and simulations. *Phys. Plasmas* **8**, 3865–3868.

BAROUD, C. N., PLAPP, B. B., SHE, Z. S. & SWINNEY, H. L. 2002 Anomalous self-similarity in a turbulent rapidly rotating fluid. *Phys. Rev. Lett.* **88**, 114501.

BENZI, R., PATARNELLO, S. & SANTANGELO, P. 1988 Self-similar coherent structures in two-dimensional decaying turbulence. *J. Phys.* A **21**, 1221–1237.

BETTEGA, G., POZZOLI, R. & ROMÉ, M. 2009 Multiresolution analysis of the two-dimensional free decaying turbulence in a pure electron plasma. *New J. Phys.* **11**, 053006.

VAN BOKHOVEN, L. J. A., TRIELING, R. R., CLERCKX, H. J. H. & VAN HEIJST, G. J. F. 2007 Influence of initial conditions on decaying two-dimensional turbulence. *Phys. Fluids* **19**, 046601.

BORGOGNO, D., CALIFANO, F., FAGANELLO, M. & PEGORARO, F. 2015 Double-reconnected magnetic structures driven by Kelvin–Helmholtz vortices at the Earth's magnetosphere. *Phys. Plasmas* **22**, 032301.

CARNEVALE, G. F., MCWILLIAMS, J. C., POMEAU, Y., WEISS, J. B. & YOUNG, W. R. 1991 Evolution of vortex statistics in two-dimensional turbulence. *Phys. Rev. Lett.* **66**, 2735–2737.

COPPA, G. G. M., PEANO, F. & PEINETTI, F. 2002 Image-charge method for contour dynamics in systems with cylindrical boundaries. *J. Comput. Phys.* **182**, 392–417.

DAVIDSON, R. C. 1990 *An Introduction to the Physics of Nonneutral Plasmas*. Addison-Wesley.

DELZANNO, G. L., LAPENTA, G. & FINN, J. M. 2002 KANDINSKY: a PIC code for fluid simulations of Penning traps. *IEEE Trans. Plasma Sci.* **30**, 34–35.

DRISCOLL, C. F. & FINE, K. S. 1990 Experiments on vortex dynamics in pure electron plasmas. *Phys. Fluids* B **2**, 1359–1366.

DRISCOLL, C. F., JIN, D. Z., SCHECTER, D. A., MOREAU, E. J. & DUBIN, D. H. E. 2000 Dynamics, statistics and vortex crystals in the relaxation of 2D turbulence. *Phys. Scr.* **84**, 76–80.

DRISCOLL, C. F., SCHECTER, D. A., JIN, D. Z., DUBIN, D. H. E., FINE, K. S. & CASS, A. C. 1999 Relaxation of 2D turbulence to vortex crystals. *Physica* A **263**, 284–292.

DRITSCHEL, D. G. & WAUGH, D. W. 1992 Quantification of the inelastic interaction of unequal vortices in two-dimensional vortex dynamics. *Phys. Fluids* A **4**, 1737–1744.

DURKIN, D. & FAJANS, J. 2000 Experiments on two-dimensional vortex patterns. *Phys. Fluids* **12** (2), 289–293.

FARGE, M. 1992 Wavelet transforms and their applications to turbulence. *Annu. Rev. Fluid Mech.* **24**, 395–457.

FARGE, M., SCHNEIDER, K. & KEVLAHAN, N. 1999 Non-gaussianity and coherent vortex simulation for two-dimensional turbulence using an adaptive orthogonal wavelet basis. *Phys. Fluids* **11** (8), 2187–2201.

FRISCH, U. 1995 *Turbulence: The Legacy of A. N. Kolmogorov*. Cambridge University Press.

HOCKNEY, R. W. & EASTWOOD, J. W. 1981 *Computer Simulation Using Particles*. McGraw-Hill.

HUANG, X.-P. & DRISCOLL, C. F. 1994 Relaxation of 2D turbulence to a metaequilibrium near the minimum enstrophy state. *Phys. Rev. Lett.* **72**, 2187–2190.

JIN, D. Z. & DUBIN, D. H. E. 1998 Regional maximum entropy theory of vortex crystal formation. *Phys. Rev. Lett.* **80**, 4434–4437.

JIN, D. Z. & DUBIN, D. H. E. 2000 Characteristics of two-dimensional turbulence that self-organizes into vortex crystals. *Phys. Rev. Lett.* **84**, 1443–1446.

KALELKAR, C. 2005 Structural studies of decaying fluid turbulence: effect of initial conditions. *Phys. Rev.* E **72**, 056307.

LEITH, C. E. 1968 Diffusion approximation for two-dimensional turbulence. *Phys. Fluids* **11**, 671–673.

LEITH, C. E. 1984 Minimum enstrophy vortices. *Phys. Fluids* **27**, 1388–1395.

LEPRETI, F., ROMÉ, M., MAERO, G., PAROLI, B., POZZOLI, R. & CARBONE, V. 2013 Scaling properties and intermittency of two-dimensional turbulence in pure electron plasmas. *Phys. Rev.* E **87**, 063110.

https://doi.org/10.1017/S0022377815000859 Published online by Cambridge University Press

LEVY, R. H. 1965 Diocotron instability in a cylindrical geometry. *Phys. Fluids* **8**, 1288–1295.
MAERO, G., ROMÉ, M., LEPRETI, F. & CAVENAGO, M. 2014 Numerical study of a dust-contaminated electron plasma. *Eur. Phys. J.* D **68**, 277.
MAGGIORE, M., CAVENAGO, M., COMUNIAN, M., CHIRULOTTO, F., GALATÀ, A., DE LAZZARI, M., PORCELLATO, A. M., RONCOLATO, C., STARK, S., CARUSO, A., LONGHITANO, A., CAVALIERE, F., MAERO, G., PAROLI, B., POZZOLI, R. & ROMÉ, M. 2014 Plasma-beam traps and radiofrequency quadrupole beam coolers. *Rev. Sci. Instrum.* **85**, 02B909.
MALLAT, S. G. 1999 *A Wavelet Tour of Signal Processing*. Academic.
MALMBERG, J. H. & DEGRASSIE, J. S. 1975 Properties of nonneutral plasma. *Phys. Rev. Lett.* **35**, 577–580.
MATSUMOTO, M. & NISHIMURA, T. 1998 Mersenne Twister: a 623-dimensionally equidistributed uniform pseudorandom number generator. *ACM Trans. Model. Comput. Simul.* **8**, 3–30.
MELANDER, M. V., ZABUSKY, N. J. & MCWILLIAMS, J. C. 1988 Symmetric vortex merger in two dimensions: causes and conditions. *J. Fluid Mech.* **195**, 303–340.
MILLER, J. 1990 Statistical mechanics of Euler equations in two dimensions. *Phys. Rev. Lett.* **65**, 2137–2140.
MILLER, J., WEICHMAN, P. B. & CROSS, M. C. 1992 Statistical mechanics, Euler's equation, and Jupiter's Red Spot. *Phys. Rev.* A **45**, 2328–2359.
MORRISON, P. J. 1984 Hamiltonian formulation of reduced magnetohydrodynamics. *Phys. Fluids* **27**, 886–897.
PEURRUNG, A. J. & FAJANS, J. 1993 Experimental dynamics of an annulus of vorticity in a pure electron plasma. *Phys. Fluids* A **5**, 493–499.
RIVERA, M., VOROBIEFF, P. & ECKE, R. E. 1998 Turbulence in flowing soap films: velocity, vorticity, and thickness fields. *Phys. Rev. Lett.* **81**, 1417–1420.
ROBERT, R. & SOMMERIA, J. 1991 Statistical equilibrium states for two-dimensional flows. *J. Fluid Mech.* **229**, 291–310.
RODGERS, D. J., SERVIDIO, S., MATTHAEUS, W. H., MONTGOMERY, D. C., MITCHELL, T. B. & AZIZ, T. 2009 Hydrodynamic relaxation of an electron plasma to a near-maximum entropy state. *Phys. Rev. Lett.* **102**, 244501.
ROMÉ, M., BRUNETTI, M., CALIFANO, F., PEGORARO, F. & POZZOLI, R. 2000 Motion of extended vortices in an inhomogeneous pure electron plasma. *Phys. Plasmas* **7**, 2856–2865.
ROMÉ, M., CAVALIERE, F., CAVENAGO, M., CHEN, S. & MAERO, G. 2015 Effects of dust contamination on the transverse dynamics of a magnetized electron plasma. In *Non-Neutral Plasma Physics IX*, *AIP Conf. Proc.* **1668**, 030001.
ROMÉ, M. & LEPRETI, F. 2011 Turbulence and coherent structures in non-neutral plasmas. *Eur. Phys. J. Plus* **126**, 38.
RUPPERT-FELSOT, J., FARGE, M. & PETITJEANS, P. 2009 Wavelet tools to study intermittency: application to vortex bursting. *J. Fluid Mech.* **636**, 427–453.
RUTGERS, M. A. 1998 Forced 2D turbulence: experimental evidence of simultaneous inverse energy and forward enstrophy cascades. *Phys. Rev. Lett.* **81**, 2244–2247.
SANTANGELO, P., BENZI, R. & LEGRAS, B. 1989 The generation of vortices in high resolution, two-dimensional decaying turbulence, and the influence of initial conditions on the breaking of self-similarity. *Phys. Fluids* A **1**, 1027–1034.
SCHECTER, D. A., DUBIN, D. H. E., FINE, K. S. & DRISCOLL, C. F. 1999 Vortex crystals from 2D Euler flow: experiment and simulation. *Phys. Fluids* **11**, 905–914.
TRIELING, R. R., VELASCO FUENTES, O. U. & VAN HEIJST, G. J. F. 2005 Interaction of two unequal corotating vortices. *Phys. Fluids* **17**, 087103.
WAUGH, D. W. 1992 The efficiency of symmetric vortex merger. *Phys. Fluids* A **4**, 1745–1758.
WEISS, J. B. & MCWILLIAMS, J. C. 1993 Temporal scaling behavior of decaying two-dimensional turbulence. *Phys. Fluids* A **5**, 608–621.
YATSUYANAGI, Y., KIWAMOTO, Y., EBISUZAKI, T., HATORI, T. & KATO, T. 2003 Simulations of diocotron instability using a special-purpose computer, MDGRAPE-2. *Phys. Plasmas* **10**, 3188–3195.
YIN, Z., MONTGOMERY, D. C. & CLERCKX, H. J. H. 2003 Alternative statistical mechanical descriptions of decaying two-dimensional turbulence in terms of patches and points. *Phys. Fluids* **15**, 1937–1953.

https://doi.org/10.1017/S0022377815000859 Published online by Cambridge University Press